Boundary effects on the plastic flow of amorphous layers during high-energy heavy-ion irradiation

A. Hedler,[1] S. Klaumünzer,[2] and W. Wesch[1]
[1]*Institut für Festkörperphysik, Friedrich-Schiller-Universität Jena, Max-Wien-Platz 1, D-07743 Jena, Germany*
[2]*Hahn-Meitner-Institut, Glienicker Strasse 100, D-14109 Berlin, Germany*
(Received 3 February 2005; revised manuscript received 17 June 2005; published 3 August 2005)

Swift heavy-ion irradiation of amorphous materials causes nonsaturating plastic deformation. Thin samples deform anisotropically as if they were hammered. Thick samples or thin layers on top of thick crystalline substrates flow plastically during nonperpendicular irradiations. In this paper, we demonstrate that the constitutive equation of ion hammering not only describes the homogeneous flow of uniformly irradiated matter but also the deformation effects at boundaries between irradiated and unirradiated matter. An analytic expression is derived which describes the flow of thin surface layers in the vicinity of an abrupt boundary. This solution is complemented by finite-element calculations, which reveal the influence of finite transition widths. The constitutive equation is also solved numerically to unveil the boundary effects for thick samples, where the ion-induced deformation depends on the distance from the specimen surface. The calculations are compared with experiments carried out with thin amorphous silicon surface layers and thick crown glasses. The excellent agreement confirms the validity of the constitutive equation and supports its microscopic basis, namely the idea of an efficient relaxation of thermally induced shear stresses along the ion path during the thermal spike period.

DOI: 10.1103/PhysRevB.72.054108 PACS number(s): 61.43.Dq, 61.80.Jh, 62.20.Dc, 68.35.Bs

I. INTRODUCTION

A swift heavy ion, penetrating a solid, predominantly interacts with the electrons of the solid giving rise to the so-called electronic energy loss per path length S_e. A high density of electronic excitations and ionizations is created a few nanometers around the ion's trajectory in less than 10^{-16} s. Depending on the degree of excitation and the specific nature of the solid, there are various routes to transform this electronic excitation energy into atomic motion. The most frequently discussed mechanisms are Coulomb explosion, nonthermal melting, and electron-phonon coupling. There is growing experimental evidence that, on the picosecond time scale, the resulting atomic motion can be adequately described as a thermal spike.[1–3]

Two decades ago, the discovery of an anisotropic growth effect in amorphous materials during high-energy heavy-ion irradiation[4–9] opened new and promising ways to contribute to the understanding of this thermal spike[9–19] and to modify amorphous materials in a well-defined way.[20–23] By means of this effect, both effective structuring and smoothing of the surfaces of amorphous layers without mass loss could be achieved.[24–27] Recently, this effect was successfully applied to shape nanoparticles for potential opto-electronic devices[28–34] and to provide experimental evidence for liquid polymorphism in silicon.[35]

The underlying phenomenon is a nonsaturating irreversible macroscopic deformation of amorphous materials during swift heavy-ion irradiation without a change in volume or mass density. Under perpendicular ion incidence, thin free-standing samples shrink parallel and grow perpendicular to the beam direction. The deformation yield, which is the relative length change per unit fluence, increases with decreasing temperature. Figuratively, the ion beam acts like a hammer and, therefore, the anisotropic growth became known as ion-hammering effect. Thick free-standing samples undergo the same effect but eventually bend due to an apparent depth dependence of the deformation yield. Ion hammering does not appear in nonamorphizable materials and the deformation of an amorphous layer on top of a thick inert substrate is mechanically constrained. However, under nonperpendicular ion incidence even thin surface layers exhibit nonsaturable shear flow as a consequence of the ion-hammering effect.

II. MODELING OF ION HAMMERING

The most successful microscopic model to describe the ion-hammering effect is the effective-flow-temperature approach by Trinkaus and Ryazanov[15] and Trinkaus.[16–19] The authors assume a thermal spike with dimensions of some nanometer in diameter and several micrometers in length. With increasing temperature, thermal expansion in combination with track confinement due to the surrounding cold matrix leads to thermal stress. At sufficiently large excitation densities, the authors postulate that the matter in the track becomes fluid. As soon as the shear viscosity in the ion track becomes sufficiently low—i.e., as soon as the temperature in the track exceeds an effective flow temperature T^*—shear-stress relaxation rapidly proceeds towards hydrostatic pressure, the state of mechanical equilibrium. As in any material, the thermal strain is reverted during cooling down to ambient temperatures, but in amorphous materials the strain increment $\varepsilon^R(t)$ associated with the shear-stress relaxation freezes-in at T^* at the solidification front $R(t)$, because there is no memory for the starting state. In nonamorphizable crystalline materials, $\varepsilon^R(t)$ is reverted by the subsequent recrystallization and no hammering can occur. By applying Eshelby's theory of elastic inclusions to the low-viscosity zone,[36] and averaging the deformation effects according to

fundamental theorems on inclusions,[37] Trinkaus and Ryazanov derived for amorphous samples, free of macroscopic stress, an asymptotic expression for the ion-hammering tensor $\underline{\underline{A}}$ for low sample temperatures, $T_0 \ll T^*$, and intense electronic excitations, $S_e \gg S_{e0}$, where S_{e0} refers to the energy deposition threshold for ion hammering. In a Cartesian coordinate system where the z axis points along the ion-track axis, $\underline{\underline{A}}$ is given by[15,38]

$$\underline{\underline{A}} = A_0 \begin{pmatrix} 1 & 0 & 0 \\ 0 & 1 & 0 \\ 0 & 0 & -2 \end{pmatrix} = \varepsilon_m^R \pi R_{\max}^2 \begin{pmatrix} 1 & 0 & 0 \\ 0 & 1 & 0 \\ 0 & 0 & -2 \end{pmatrix}, \quad (1)$$

where A_0 is the deformation yield per ion, ε_m^R the mean frozen-in relaxation strain and R_{max} the maximum radius of the low-viscosity zone. For a Gaussian temperature profile, set up by the fraction gS_e, the maximum cross section of the low-viscosity zone reads

$$\pi R_{\max}^2 = \frac{gS_e}{e\varrho C \Delta T^*}, \quad (2)$$

where ϱ and C represent effective values for the density and specific heat of the material, respectively, $\Delta T^* = T^* - T_0$, and $e = 2.718$ is the base of the natural logarithm. In the case of a constant linear thermal expansion coefficient α the deformation yield A_0 is given by[15]

$$A_0 = 1.164 \frac{1+\nu}{5-4\nu} \frac{\alpha g S_e}{e\varrho C}, \quad (3)$$

where ν is the Poisson number. In the case of thick layers, S_e varies along the penetration path ξ, hence $A_0(\xi) \propto S_e(\xi)$.[39]

As a consequence of multiple ion impacts, the ion-hammering strain rate is given by

$$\dot{\underline{\underline{\varepsilon}}}^I = \underline{\underline{A}} \Phi, \quad (4)$$

where Φ is the ion flux. Because of $\hat{A} = \mathrm{Tr}(\underline{\underline{A}}) = 0$, ion hammering occurs without density change. In a Cartesian coordinate system as depicted in Fig. 1, $\dot{\underline{\underline{\varepsilon}}}^I$ is given by[24,40]

$$\dot{\underline{\underline{\varepsilon}}}^I = A_0 \Phi \begin{pmatrix} 1 - 3\sin^2\Theta & 0 & 3\sin\Theta\cos\Theta \\ 0 & 1 & 0 \\ 3\sin\Theta\cos\Theta & 0 & 1 - 3\cos^2\Theta \end{pmatrix}, \quad (5)$$

where Θ stands for the incidence angle of the ions measured from the surface normal of the sample.

When a mechanical stress $\underline{\underline{\sigma}}$ is present, either applied externally or induced by the constraints of an unirradiated or crystalline environment, ion hammering is superimposed by a creep term proportional to the stress deviator $\tilde{\underline{\underline{\sigma}}} = \underline{\underline{\sigma}} - \hat{\sigma}/3\ \underline{\underline{I}}$, with $\hat{\sigma} = \mathrm{Tr}(\underline{\underline{\sigma}})$ and $\underline{\underline{I}}$ the unity tensor.[17,22,42–44] This apparent Newtonian flow with strain rate $\dot{\underline{\underline{\varepsilon}}}^N$ is described by a totally symmetric effective fluidity tensor of rank four $\underline{\underline{\underline{\underline{k}}}}\Phi$ according to[24,33,45,46]

$$\dot{\underline{\underline{\varepsilon}}}^N = \underline{\underline{\underline{\underline{k}}}}[S_e(\xi)] \Phi \tilde{\underline{\underline{\sigma}}}. \quad (6)$$

The total strain rate of the irradiated amorphous sample $\dot{\underline{\underline{\varepsilon}}}$ is given by a modified Maxwell model[24,33,45,46]

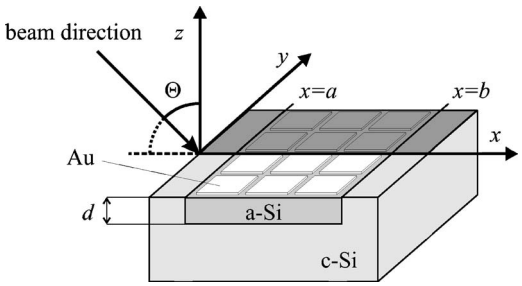

FIG. 1. Schematic view of the irradiation geometry with a y boundary in the case of an embedded amorphous silicon (a-Si) layer of thickness d in crystalline silicon (c-Si). The projection of the ion beam onto the specimen surface determines the x axis. The x axis is the borderline between irradiated area ($y<0$) and unirradiated area ($y>0$). The surface of the unirradiated specimen part defines $z=0$ and the incidence angle of the ions Θ is measured from the z axis. The same notation is used for the irradiation of the crown glass. For $y \to -\infty$, the transition from c-Si to a-Si at $x=a$ forms an x_a boundary and the transition from a-Si to c-Si at $x=b$ forms an x_b boundary since c-Si is almost inert to irradiation with swift heavy ions (Ref. 41).

$$\dot{\underline{\underline{\varepsilon}}} = \dot{\underline{\underline{\varepsilon}}}^I + \dot{\underline{\underline{\varepsilon}}}^H + \dot{\underline{\underline{\varepsilon}}}^N. \quad (7)$$

The strain rate $\dot{\underline{\underline{\varepsilon}}}^H$ describes purely elastic behavior according to Hooke's law, which reads for isotropic compressible materials

$$\dot{\varepsilon}_{ij}^H = \frac{1}{2G} \frac{d}{dt} \left(\sigma_{ij} - \frac{\nu}{\nu+1} \hat{\sigma} \delta_{ij} \right), \quad (8)$$

with the shear modulus G. The strain rate $\dot{\underline{\underline{\varepsilon}}}$ is linked to the velocity $\underline{v}$ by

$$\dot{\varepsilon}_{ij} = \frac{1}{2} \left(\frac{\partial v_i}{\partial x_j} + \frac{\partial v_j}{\partial x_i} \right). \quad (9)$$

The constitutive equation of the viscoelastic model, Eq. (7), is supplemented by the equation of motion. For small velocities of some nm/s, the inertia terms can be ignored and the equation of motion reduces to quasistatic equilibrium

$$\mathrm{Div}\ \underline{\underline{\sigma}} = 0. \quad (10)$$

The macroscopic deformation state of the sample can be derived by solving Eqs. (5)–(10) for the nine quantities v_i and σ_{ij} and taking into account initial and boundary conditions as well as irradiation-induced symmetry relations in the irradiated area. A general solution of this system of equations is probably impossible. Therefore, in this paper we assume that the sample fills the half-space $z \leqslant 0$ and we consider three cases (cf. Fig. 1): (i) Far away from any boundary and for uniform irradiation, i.e., $\Phi(x,y) = \Phi_0$, we have $\underline{v} = \underline{v}(z,t)$ and $\underline{\underline{\sigma}} = \underline{\underline{\sigma}}(z,t)$; in the following this region will be denoted as "central region." (ii) If the ion flux is collimated to the region $y \leqslant 0$, i.e., a boundary is running along the x axis, we have $\Phi = \Phi(y)$, $\underline{v} = \underline{v}(y,z,t)$, and $\underline{\underline{\sigma}} = \underline{\underline{\sigma}}(y,z,t)$. Such a boundary will be called "y boundary." (iii) If the ion flux is collimated to the region $x \geqslant a$, i.e., a boundary is running parallel to the y axis, we have $\Phi = \Phi(x)$, $\underline{v} = \underline{v}(x,z,t)$, and $\underline{\underline{\sigma}} = \underline{\underline{\sigma}}(x,z,t)$. Such a boundary will be called "x_a boundary." Similarly, if the flux

is collimated to $x \leqslant b$, we call the corresponding boundary an "x_b boundary."

Furthermore, we rigorously simplify Eq. (6) by replacing $\underline{\underline{k}}$ by its scalar part k_0. According to Trinkaus, k_0 results from the scalar component F_0 of the normalized fluidity tensor $\underline{\underline{F}}$ according to[17]

$$k_0 = \frac{F_0}{2G}\pi R_{\max}^2 = \frac{33-47\nu+16\nu^2}{5G(5-4\nu)}\frac{gS_e}{e\varrho C\Delta T^*} \equiv \frac{1}{2\eta_{rad}}, \tag{11}$$

so that η_{rad} (in Pa ion/cm^2) describes a flux-independent radiation-induced viscosity.[42–44,46] With these approximations the shear velocity in the central region is given by[24,45,46]

$$v_x(z) = 3\Phi_0 \sin 2\Theta \cos\Theta \int_{\xi_0}^{z/\cos\Theta} A_0[S_e(\xi)]d\xi, \tag{12}$$

where ξ_0 denotes the maximum deformation length. The integration of Eq. (12) over time yields the shift $\Delta x(z,t)$ in the central region, which at the surface of a thin amorphous layer with thickness d is given by[24,45,46]

$$\Delta x(z=0,t) = 3dA_0(S_e)\Phi_0 t \sin 2\Theta, \tag{13}$$

where $\Phi_0 t$ is the uniform ion fluence in the central region.

This description of the ion-hammering effect and its macroscopic consequences is in good agreement with experimental observations.[15,33,35] However, the model has not yet been verified for the reduction of the shear velocity and the formation of ditch and dike structures at y and x boundaries, respectively. In this paper we demonstrate that the viscoelastic model also applies to these stress-induced deformation effects in areas with low symmetry.

III. EXPERIMENTS

The experiments were performed with amorphous silicon (a-Si) surface layers, 3×3 mm^2 in size, and samples of a crown glass (B270, Deutsche Spezialglas AG), 5×5 mm^2 in size, representing thin amorphous surface layers on top of crystalline substrates and thick amorphous layers, respectively. The a-Si surface layers were produced by multiple Si ion implantation into 370-μm-thick crystalline silicon (c-Si) wafers at 100 K using various ion energies between 0.25 MeV and 9.5 MeV and ion fluences in the range between 3×10^{15} cm^{-2} and 7×10^{15} cm^{-2}. The implantations were carried out at the Tandetron accelerator of the University of Jena. Rutherford backscattering spectrometry, infrared-reflection spectrometry, and cross-sectional transmission electron microscopy revealed a homogeneous amorphous surface layer, free of voids and hydrogen, with a thickness of $d=(5.71\pm0.05)$ μm. Its material parameters are $\varrho=2.29$ g/cm^3, $G=38.8$ GPa, and $\nu=0.29$. Because a-Si is about 1.8% less dense than c-Si,[47] amorphization of c-Si results in both building up of biaxial in-plane compressive stresses and out-of-plane swelling. After complete amorphization, further implantation induces a relaxation of these in-plane stresses. If they were completely vanished, height changes of about 100 nm would have been expected. However, DEKTAK line scans revealed an initial out-of-plane swelling of a-Si with respect to c-Si of about 80 nm. In effect, the remaining biaxial in-plane stresses prior to the swift heavy-ion irradiations can be estimated to be about $\sigma_0 \sim -0.3$ GPa in agreement with values derived from curvature measurements.[48] Before irradiation with swift heavy ions, a Au layer of approximately 40 nm thickness was evaporated onto the sample surface through a Ni net in order to quantify irradiation-induced plastic flow with a precision of 1 μm.

TABLE I. Swift heavy-ion irradiation conditions. The incidence angle of the ions was kept at $\Theta=45^\circ$.

	Irradiation	T_0 (K)	Φ_0 (10^{10} cm^{-2} s^{-1})	$\Phi_0 t$ (10^{15} cm^{-2})
a-Si	390 MeV Xe	80	6.3	7.4
a-Si	390 MeV Xe	300	8.3	9.3
a-Si	350 MeV Au	80	4.6	1.7
a-Si	350 MeV Au	300	2.5	0.8
a-Si	600 MeV Au	80	5.7	3.1
a-Si	600 MeV Au	300	5.3	2.6
B270	600 MeV Au	300	4.3	0.3
B270	600 MeV Au	300	4.4	0.1

The 1.5-mm-thick crown glass samples were provided with scaled surfaces by the Heidenhain Company, Germany. The composition in wt % of the crown glass was 69.5 SiO_2; 8.3 K_2O; 8.1 Na_2O; 7.1 CaO; 4.2 ZnO; 2.1 BaO; 0.5 TiO_2, and 0.5 Sb_2O_3. Its material parameters are $\varrho=2.55$ g/cm^3, $G=29.3$ GPa, $\nu=0.22$, $\alpha_{20-500^\circ\,C}=10.3\times10^{-6}$ K^{-1}, and $C=0.86$ J/g K.

Swift heavy-ion irradiations were carried out at the Ion Beam Laboratory ISL in Berlin using 390 MeV Xe^{21+}, 350 MeV Au^{26+}, and 600 MeV Au^{30+} ions with a homogeneous beam sweep of 5×5 mm^2 and the conditions listed in Table I. The irradiation geometry is shown in Fig. 1. In front of the samples there were apertures so that a part of each sample remained unirradiated. The borderlines between irradiated and unirradiated specimen parts formed y boundaries. In the case of a-Si embedded in c-Si, the interfaces to c-Si formed x boundaries since c-Si is almost inert to swift heavy-ion irradiation.[41] In fact, the aperture was movable and micrographs of the sample surfaces were taken *in situ* with a long-distance microscope.

The electronic energy depositions per unit path length $S_e(\xi)$ of the ion-target combinations used in our experiments are shown in Fig. 2. It can be seen that $S_e(\xi)$ is nearly constant across the a-Si layer with a maximum deformation length of $\xi_0=-d/\cos\Theta \sim -8.1$ μm [Fig. 2(a)]. The mean values S_e are listed in Table II. In the case of the crown glass, $S_e(\xi)$ can be fitted by a fourth-order polynomial fit. The numerical values with the appropriate units are given in Fig. 2(b).

The irradiated samples were analyzed by means of a stylus profilometer (DEKTAK), atomic force microscopy (AFM), laser profilometry (LP), and scanning electron microscopy (SEM).

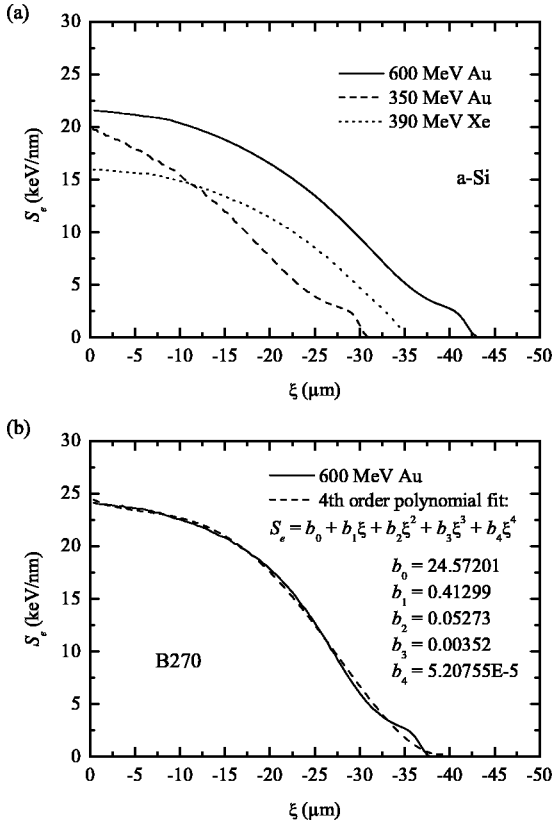

FIG. 2. Electronic energy deposition per unit path length $S_e(\xi)$ of a penetrating ion for the irradiation conditions used in our experiments in the case of a-Si (a) and the crown glass (b). The distributions were calculated with SRIM2003 (Ref. 49).

IV. EXPERIMENTAL RESULTS

During swift heavy-ion irradiation a-Si flows plastically in the same way as conventional glasses.[35,50] As an example, Fig. 3 shows the shift at the specimen surface in the uniformly irradiated central region $\Delta x(z=0,t)$ as a function of the ion fluence $\Phi_0 t$ for 600 MeV Au irradiation at $T_0 = 80$ K. In accordance with Eq. (13), $\Delta x(z=0,t)$ increases linearly with $\Phi_0 t$ at $T_0=80$ K, whereas at $T_0=300$ K a linear behavior is only found for low fluences.[50] By applying Eq. (13), the deformation yields $A_0(S_e)$ were derived and the results are summarized in Table II.

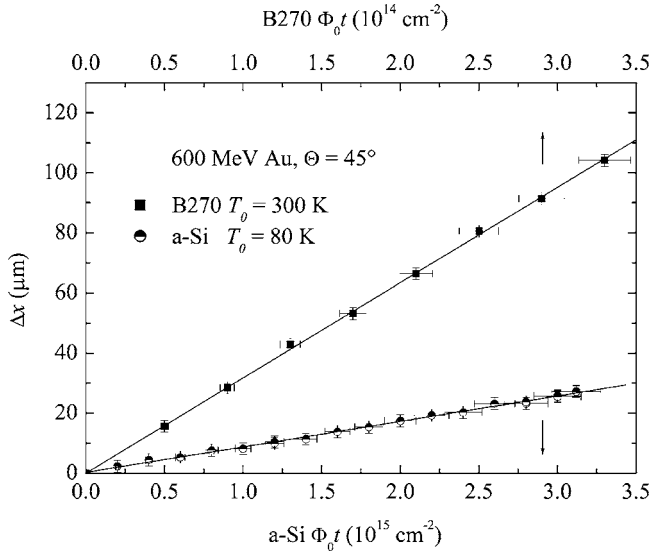

FIG. 3. Shift at the surface $\Delta x(z=0,t)$ in the uniformly irradiated central region versus ion fluence $\Phi_0 t$ during 600 MeV Au irradiation of a-Si at $T_0=80$ K and the crown glass at $T_0=300$ K.

In the vicinity of a y boundary the shift depends on the distance from the boundary and vanishes in the unirradiated area (cf. Fig. 8).[35,50] DEKTAK line scans across the y boundary of a-Si revealed no remarkable height changes. Thus, irradiation-induced density changes are below 1% for irradiations with swift heavy ions at $T_0=80$ K, or $T_0=300$ K and low fluences, respectively.[50]

Figure 4 shows a DEKTAK line scan parallel to the x axis of an a-Si sample after an irradiation with 390 MeV Xe ions at $T_0=300$ K. As a consequence of the lateral mass transport in the positive x direction, a ditch (dike) appear at the x_a (x_b) boundary. The depth (height) and cross section of the ditch (dike) changed continuously with the ion fluence. No steady state of these deformations was observed. In Table II, the values of the cross sections for the ditch, F_d, and dike, F_D, derived from long-scan DEKTAK profiles are listed for the corresponding irradiation conditions.

In Fig. 5, a comparison of the DEKTAK profiles at the x boundaries from Fig. 4 with measurements by AFM is shown. Due to the resolution limit given by the stylus width, DEKTAK cannot resolve the exact depth and shape of narrow

TABLE II. Electronic energy deposition S_e, deformation yield A_0, and cross sections of ditch F_d and dike F_D at the x_a and x_b boundaries, respectively, for the irradiations of a-Si. The cross sections were derived from DEKTAK surface profilometry. Also the mean value $F_m=(F_d+F_D)/2$ is listed together with the cross section of the uniform flow in the central region F_c and the relative deviation $\Delta F/F_c=(F_m-F_c)/F_c$.

Irradiation	S_e (keV/nm)	T_0 (K)	Φ_{0t} (10^{15} cm^{-2})	A_0 (10^{-16} cm^2)	F_d (μm^2)	F_D (μm^2)	F_m (μm^2)	F_c (μm^2)	$\Delta F/F_c$ (%)
390 MeV Xe	15.8±0.2	80	7.4	1.2	28	54	41	43	−5
390 MeV Xe	15.8±0.2	300	9.3	0.9	29	63	46	41	12
350 MeV Au	18.8±1.0	80	1.7	3.7	26	32	29	31	−6
350 MeV Au	18.8±1.0	300	0.8	2.9	—	12	(12)	11	(9)
600 MeV Au	21.3±0.3	80	3.1	5.0	43	94	69	75	−8
600 MeV Au	21.3±0.3	300	2.6	3.5	—	31	(31)	44	(−29)

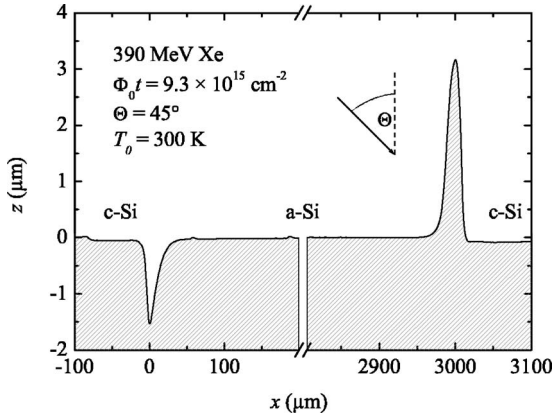

FIG. 4. DEKTAK surface profile of an a-Si layer embedded in c-Si after an irradiation with 390 MeV Xe ions at $T_0=300$ K, flux $\Phi_0=8.3\times10^{10}$ cm^{-2} s^{-1}, and fluence $\Phi_0 t=9.3\times10^{15}$ cm^{-2}. The a-Si layer extends from $x_a=0$ to $x_b=3000$ μm.

and steep structures. The underestimation of the ditch in Fig. 5(a) and the overestimation of the dike in Fig. 5(b) in comparison with the AFM measurements are clearly visible. Unfortunately, the length of the AFM line scans was limited to about 50 μm and some of the irradiations induced more than

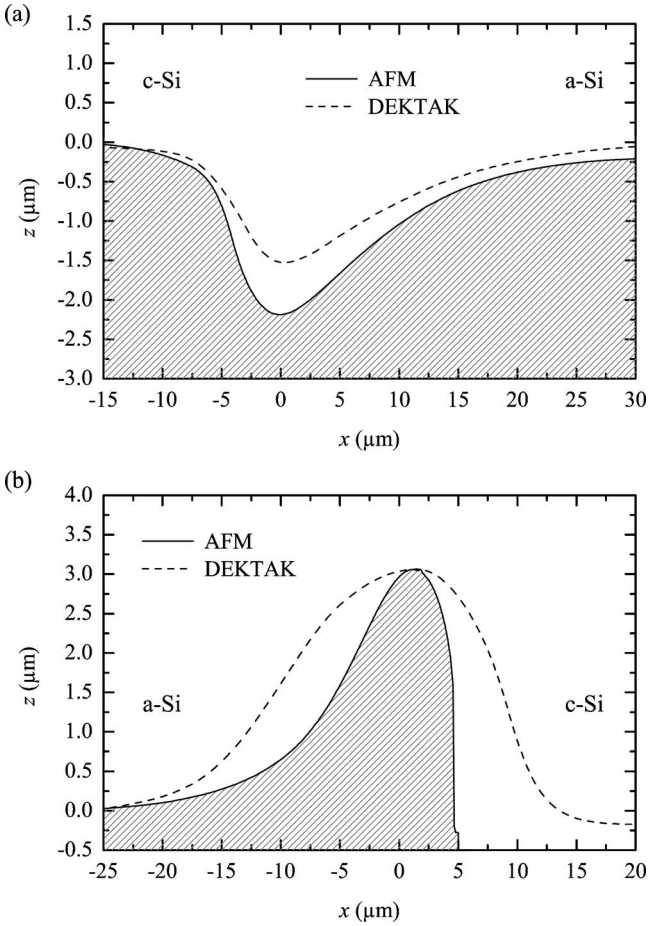

FIG. 5. DEKTAK and AFM surface profiles of the sample from Fig. 4 at the x_a boundary (a) and x_b boundary (b). The origin of the x scale is set arbitrarily.

one ditch, so that the x boundary effects could not be satisfactorily analyzed by AFM. Due to the smallness of the effects, SEM and LP did not provide more precise measurements. However, since plastic flow occurs without mass loss and with a constant shear velocity in the uniformly irradiated central region, a homogeneous mass transport is expected, i.e., the mass, which is missing at the x_a boundary, forms the dike at the x_b boundary.[24,45,46] Thus, the mean value $F_m=(F_d+F_D)/2$ represents a fair estimate for the real cross section of both ditch and dike.

For the crown glass sample, Fig. 3 shows the shift at the specimen surface in the uniformly irradiated central region, $\Delta x(z=0,t)$, versus ion fluence $\Phi_0 t$ (600 MeV Au, $T_0=300$ K). Because of the similarities with all investigated amorphous materials, it is plausible to assume that the deformation yield $A_0(S_e)$ of the crown glass also increases linearly with S_e according to

$$A_0[S_e(\xi)] = \kappa[S_e(\xi) - S_{e0}]. \tag{14}$$

Because $S_{e0}<2$ keV/nm for soda-lime glasses, we ignore S_{e0} for the crown glass and ξ_0 equals the projected ion range. Then we obtain from Eqs. (12) and (14)

$$\Delta x(z=0,t) = 3\kappa\Phi_0 t E_{ion} \sin 2\Theta \cos\Theta, \tag{15}$$

where E_{ion} is the kinetic energy of the swift heavy ion. The linear fit in Fig. 3 yields $\kappa=0.0257$ nm^3/keV. Thus, the deformation yield of the crown glass at the surface $A_0[S_e(\xi=0)]=61.8\times10^{-16}$ cm^2 is an order of magnitude higher than the one of a-Si (cf. Table II). Using $g=0.5$ from Eq. (3), a low-temperature value $\kappa=0.05$ nm^3/keV follows. An increase of κ by a factor of 2 going from $T_0=300$ K to very low temperatures is not uncommon for silicate glasses.[40]

Similarly to other glasses, at the y boundary a reduction of the surface shift occurs along the way from the uniformly irradiated central region to the unirradiated area (cf. Fig. 10). DEKTAK line scans across the y boundary revealed step heights of about 300 nm for a fluence of 1×10^{14} cm^{-2}. Thus, irradiation-induced density changes are below 1% as in the case of a-Si. Because the samples were irradiated over their whole widths, x boundaries were absent and the formation of ditch and dike structures could not be observed.

V. DISCUSSION

A. Irradiation effects in the central region

As long as in the uniformly irradiated central region the surface remains plane, all derivatives $\partial/\partial x$ and $\partial/\partial y$ must vanish and Eqs. (7) and (10) reduce to

$$0 = \frac{1}{2G}\frac{\partial}{\partial t}\left[\sigma_{xx} - \frac{\nu}{\nu+1}\hat{\sigma}\right] + k_0\Phi_0\left[\sigma_{xx} - \frac{1}{3}\hat{\sigma}\right] + A_0\Phi_0(1 - 3\sin^2\Theta), \tag{16a}$$

$$0 = \frac{1}{2G}\frac{\partial}{\partial t}\left[\sigma_{yy} - \frac{\nu}{\nu+1}\hat{\sigma}\right] + k_0\Phi_0\left[\sigma_{yy} - \frac{1}{3}\hat{\sigma}\right] + A_0\Phi_0, \tag{16b}$$

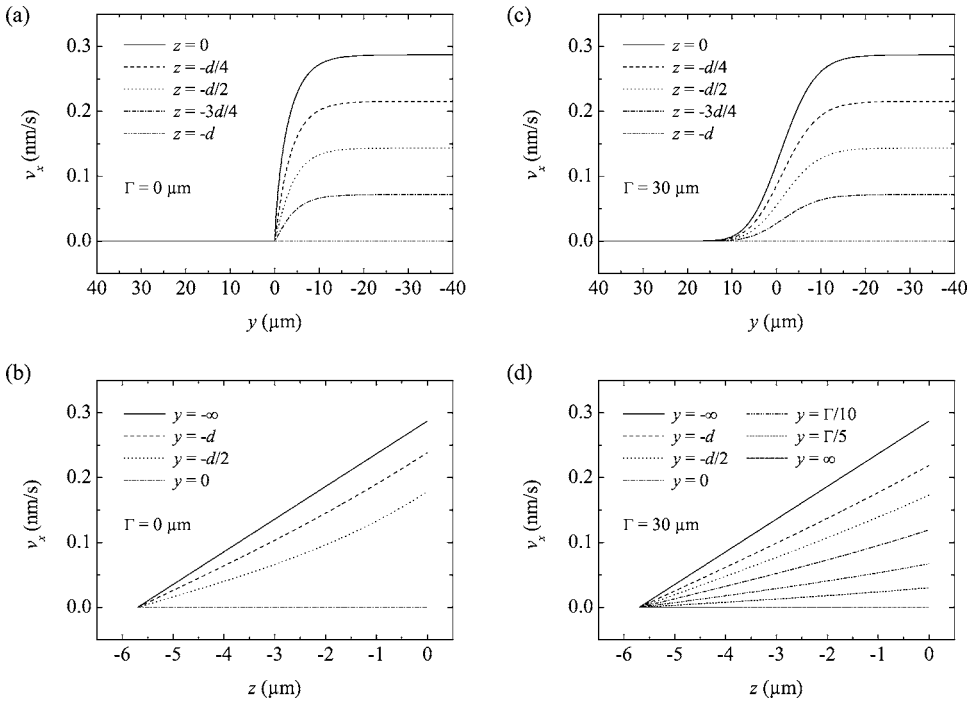

FIG. 6. Steady-state shear velocity $v_x(y,z)$ of a-Si at the y boundary with a transition width $\Gamma=0$ μm (a) and (b), and $\Gamma=30$ μm (c) and (d), respectively. (a) and (c) show $v_x(y)$ for constant values z and (b) and (d) show $v_x(z)$ for constant values y. The numerical and analytical calculations coincide in (a) and (b). All calculations were carried out for $d=5.7$-μm-thick a-Si layer irradiated with 350 MeV Au ions at $T_0=80$ K and ion flux $\Phi_0=4.6\times10^{10}$ cm^{-2} s^{-1}.

$$\frac{\partial v_z}{\partial z} = \frac{1}{2G}\frac{\partial}{\partial t}\left[\sigma_{zz} - \frac{\nu}{\nu+1}\hat{\sigma}\right] + k_0\Phi_0\left[\sigma_{zz} - \frac{1}{3}\hat{\sigma}\right] + A_0\Phi_0(1-3\cos^2\Theta), \tag{16c}$$

$$0 = \frac{1}{2G}\frac{\partial}{\partial t}\sigma_{xy} + k_0\Phi_0\sigma_{xy}, \tag{16d}$$

$$\frac{1}{2}\frac{\partial v_x}{\partial z} = \frac{1}{2G}\frac{\partial}{\partial t}\sigma_{xz} + k_0\Phi_0\sigma_{xz} + A_0\Phi_0 3\sin\Theta\cos\Theta, \tag{16e}$$

$$\frac{1}{2}\frac{\partial v_y}{\partial z} = \frac{1}{2G}\frac{\partial}{\partial t}\sigma_{yz} + k_0\Phi_0\sigma_{yz}, \tag{16f}$$

$$0 = \frac{\partial\sigma_{xz}}{\partial z} = \frac{\partial\sigma_{yz}}{\partial z} = \frac{\partial\sigma_{zz}}{\partial z}. \tag{16g}$$

The material derivative d/dt has been replaced by $\partial/\partial t$, which implies that the following considerations are limited to small shears. From Eq. (16g) and the fact that the surface is traction-free, $\sigma_{xz}=\sigma_{yz}=\sigma_{zz}=0$ holds for the entire amorphous layer thickness at all times. The initial condition is either determined by a biaxial stress field with $\sigma_{xx}(t=0)=\sigma_{yy}(t=0)=\sigma_0$ (as in the case of a-Si, see Sec. III) or given by a stress-free state with $\sigma_0=0$ (as in the case of the crown glass). With $\sigma_{xy}(t=0)=0$, Eq. (16d) immediately yields $\sigma_{xy}=0$ for all times.

The solution for the in-plane stresses results from Eqs. (16a) and (16b) and is given by

$$\sigma_{xx}(z,t) = \sigma_c\left[\beta_1 + \beta_2\exp\frac{-t}{\tau_G} + \beta_3\exp\frac{-t}{\tau_Y}\right] + \sigma_0\exp\frac{-t}{\tau_Y}, \tag{17a}$$

$$\sigma_{yy}(z,t) = \sigma_c\left[\gamma_1 + \gamma_2\exp\frac{-t}{\tau_G} + \gamma_3\exp\frac{-t}{\tau_Y}\right] + \sigma_0\exp\frac{-t}{\tau_Y}, \tag{17b}$$

where $\tau_G=1/(2Gk_0\Phi_0)$ and $\tau_Y=3/(Yk_0\Phi_0)$ correspond to time constants for stress relaxation determined by the shear modulus G and the biaxial elastic modulus $Y=2G(1+\nu)/(1-\nu)$, respectively, and $\sigma_c=-3A_0/k_0=-6A_0\eta_{rad}$ denotes the maximum steady-state compressive stress. The coefficients β_i and γ_i are given by

$$\beta_1 = \cos 2\Theta, \quad \beta_2 = \frac{1}{2}\sin^2\Theta, \quad \beta_3 = \frac{1}{2}(1-3\cos^2\Theta),$$

$$\gamma_1 = \cos^2\Theta, \quad \gamma_2 = -\frac{1}{2}\sin^2\Theta, \quad \gamma_3 = \frac{1}{2}(1-3\cos^2\Theta).$$

For $\sigma_0=0$, the stress σ_{xx} is compressive for $\Theta<45°$, is temporarily tensile for $\Theta=45°$, and vanishes completely for $t\gg\tau_Y$. For $\Theta>45°$, σ_{xx} is always tensile. The stress σ_{yy} is compressive for all Θ and at all times.

Since the unirradiated part below the bombarded region is at rest, from Eq. (16f) it follows $v_y=0$. The shear velocity v_x is immediately in a steady state, follows directly from Eq. (16e), and is given by Eq. (12). The out-of-plane velocity v_z is obtained from Eqs. (16c), (17a), and (17b)

$$v_z(z,t) = \Phi_0 \frac{1-2\nu}{1-\nu} \cos\Theta \int_{\xi_0}^{z/\cos\Theta} \left[2\beta_3 A_0 - \frac{2}{3}\sigma_0 k_0 \right] \times \exp\frac{-t}{\tau_Y} d\xi. \quad (18)$$

This motion of the specimen surface is not caused by an intrinsic radiation-induced density change but a consequence of mechanically constrained ion hammering. The integration of v_z at $z=0$ over time yields the height change $\Delta z(t)$ with respect to the unirradiated surface

$$\Delta z(t) = \Phi_0 \frac{1-2\nu}{1-\nu} \cos\Theta \int_{\xi_0}^{0} \left[2\beta_3 A_0 - \frac{2}{3}\sigma_0 k_0 \right] \times \tau_Y \left[1 - \exp\frac{-t}{\tau_Y} \right] d\xi. \quad (19)$$

In the case of $\sigma_0=0$, Δz is negative for $\Theta<55°$ and positive for $\Theta>55°$.

Taking into account that $\tau_Y > \tau_G$, the characteristic fluence for the approach of the steady state is given by

$$\Phi_0 \tau_Y = \frac{3}{Yk_0} = \frac{3}{F_0} \frac{1-\nu}{1+\nu} \frac{1}{\pi R_{\max}^2}. \quad (20)$$

In the steady state, ion hammering and stress-induced creep are in equilibrium. The corresponding stresses and the height change follow from Eqs. (17a), (17b), and (19) for $t\to\infty$ resulting in[24,45,46]

$$\sigma_{xx}(z) = -3\frac{A_0}{k_0}\cos 2\Theta, \quad (21a)$$

$$\sigma_{yy}(z) = -3\frac{A_0}{k_0}\cos^2\Theta, \quad (21b)$$

$$\Delta z = \Phi_0 \frac{1-2\nu}{1-\nu} \cos\Theta \int_{\xi_0}^{0} \left[2\beta_3 A_0 - \frac{2}{3}\sigma_0 k_0 \right] \tau_Y \, d\xi. \quad (21c)$$

Because the quantities A_0 and k_0 depend in the same way on S_e [cf. Eqs. (3) and (11)] the steady-state in-plane stresses should not be depth dependent even in thick layers.

Using a typical track radius of $R_{max}\sim 3$ nm and the corresponding material parameters, Eq. (11) yields the values $k_0\sim 0.8\times10^{-21}$ m^2/MPa and $k_0\sim 1.1\times10^{-21}$ m^2/MPa for a-Si and the crown glass, respectively. Consequently, Eq. (20) yields a characteristic fluence of $\Phi_0\tau_Y\sim 0.8/\pi R_{max}^2\sim 3\times10^{12}$ cm^{-2} for both a-Si and the crown glass, and is of the order of one complete coverage of the irradiated area with ion tracks. Furthermore, using the experimental results for A_0, by means of Eq. (21b) a steady-state compressive stress of $\sigma_{yy}\sim -0.1$ GPa and $\sigma_{yy}\sim -0.8$ GPa can be estimated for a-Si and the crown glass, respectively. These stresses are sufficiently small to be consistent with one of the basic assumptions of the effective-flow-temperature approach, namely the linearity between strains and stresses. Taking into account the initial stress states, the steady-state step height as predicted from Eq. (21c) is $\Delta z\sim 10$ nm for a-Si and $\Delta z\sim -250$ nm for the crown glass. While for a-Si the experimentally observed height change of $\Delta z<50$ nm is in good agreement with the theoretical value, for the crown glass a small swelling effect with $\Delta z\sim 300$ nm has been observed, which is obviously due to a second process, presumably defect generation with saturation of defects when track overlap is important. However, since the plastic flow of the crown glass is similar to that of all other investigated glasses we conclude that this neglected effect does not determine the steady-state flow process.

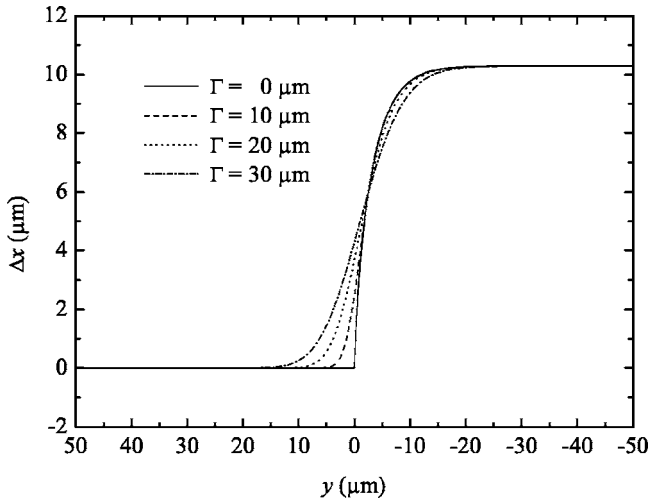

FIG. 7. Shift at the surface, $\Delta x(y,z=0,t)$, of a-Si at the y boundary for different transition widths Γ. The numerical calculations were carried out for a 5.7-μm-thick a-Si layer irradiated with 350 MeV Au ions at $T_0=80$ K, flux $\Phi_0=4.6\times10^{10}$ cm^{-2} s^{-1}, and fluence $\Phi_0 t=1.7\times10^{15}$ cm^{-2}.

B. Irradiation effects at the y boundary

In the transition region of a y boundary all derivatives $\partial/\partial x$ must vanish. Because the steady state is reached at rather small fluences we look only for such a solution for $\underline{\sigma}$ and $\underline{v}$. In this case Eqs. (7) and (10) reduce to

$$0 = k_0\Phi\left[\sigma_{xx} - \frac{1}{3}\hat{\sigma} \right] + A_0\Phi(1-3\sin^2\Theta), \quad (22a)$$

$$\frac{\partial v_y}{\partial y} = k_0\Phi\left[\sigma_{yy} - \frac{1}{3}\hat{\sigma} \right] + A_0\Phi, \quad (22b)$$

$$\frac{\partial v_z}{\partial z} = k_0\Phi\left[\sigma_{zz} - \frac{1}{3}\hat{\sigma} \right] + A_0\Phi(1-3\cos^2\Theta), \quad (22c)$$

$$\frac{1}{2}\frac{\partial v_x}{\partial y} = k_0\Phi\sigma_{xy}, \quad (22d)$$

$$\frac{1}{2}\frac{\partial v_x}{\partial z} = k_0\Phi\sigma_{xz} + A_0\Phi 3\sin\Theta\cos\Theta, \quad (22e)$$

$$\frac{1}{2}\left[\frac{\partial v_y}{\partial z} + \frac{\partial v_z}{\partial y} \right] = k_0\Phi\sigma_{yz}, \quad (22f)$$

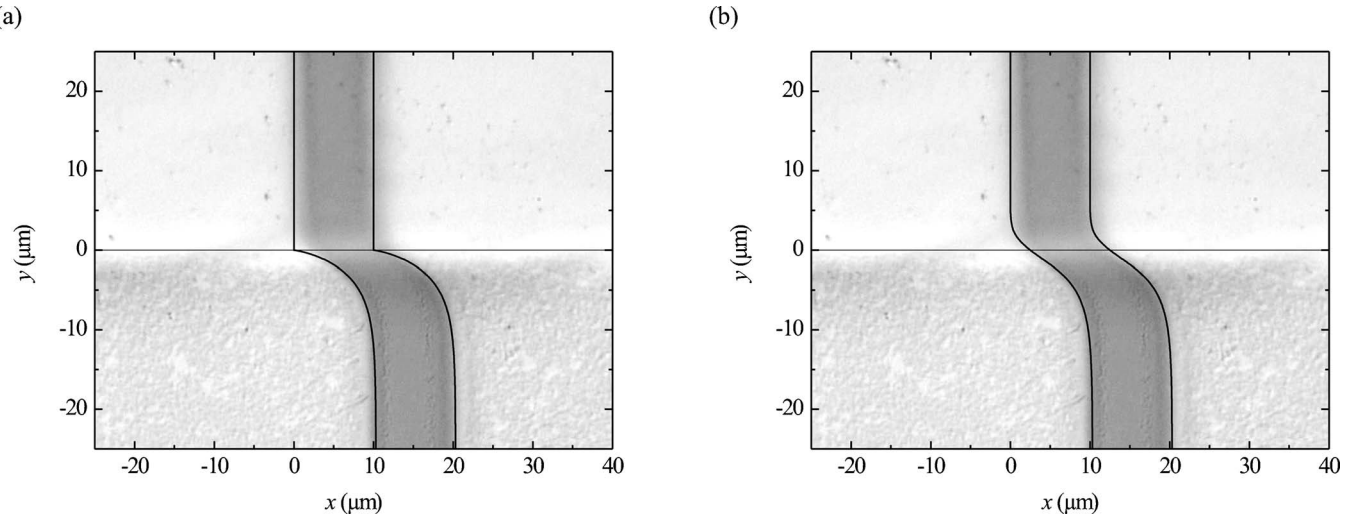

FIG. 8. Comparison of the calculated shift at the surface $\Delta x(y,z=0,t)$ of a-Si with the experimental result for a transition width $\Gamma=0$ μm (a) and $\Gamma=10$ μm (b). The underlying micrograph of the specimen surface was taken from a 5.7-μm-thick a-Si layer after an irradiation with 350 MeV Au ions at $T_0=80$ K, $\Phi_0=4.6\times10^{10}$ cm^{-2} s^{-1} and $\Phi_0 t=1.7\times10^{15}$ cm^{-2}. The calculation results were taken from Fig. 7. The origin $y=0$ is chosen to give optimal agreement with the experiment, $x=0$ is arbitrary.

$$0=\frac{\partial\sigma_{xy}}{\partial y}+\frac{\partial\sigma_{xz}}{\partial z}, \tag{22g}$$

$$0=\frac{\partial\sigma_{yy}}{\partial y}+\frac{\partial\sigma_{yz}}{\partial z}, \tag{22h}$$

$$0=\frac{\partial\sigma_{yz}}{\partial y}+\frac{\partial\sigma_{zz}}{\partial z}. \tag{22i}$$

From Eqs. (22a)–(22c) we have div $\underline{v}=0$. If $v_y\neq0$ were valid in the vicinity of the y boundary, it would follow $v_z\neq0$ and vice versa. This would lead to the formation of a ditch and/or dike structure. If the surface were no longer plane, ion hammering would modify the stress state and, in turn, would induce further flow without reaching a steady state. Therefore, a search for a steady-state solution of Eqs. (22a)–(22i) is equivalent with the condition $v_y=v_z=0$. This is exactly the situation we encounter in the experiments. As a result, Eq. (22f) yields $\sigma_{yz}=0$ and from Eqs. (22h) and (22i) we find that $\partial\sigma_{yy}/\partial y=\partial\sigma_{zz}/\partial z=0$. At the plane and traction-free surface we have $\sigma_{xz}=\sigma_{yz}=\sigma_{zz}=0$. Then from Eq. (22i) it follows that σ_{zz} must vanish in the entire y-boundary region. Inserting $\sigma_{zz}=0$ in Eqs. (22a) and (22b), we find that σ_{xx} and σ_{yy} are the same as in the central region and given by Eqs. (21a) and (21b).

According to Eqs. (22d) and (22e) the shear stresses σ_{xy} and σ_{xz} are coupled with the shear velocity v_x and, therefore, will change across the y boundary. An equation for $v_x(y,z)$ can be obtained by eliminating these shear stresses in Eq. (22g) by means of Eqs. (22d) and (22e). The result reads

$$0=\frac{\partial^2 v_x}{\partial y^2}+\frac{\partial^2 v_x}{\partial z^2}+\lambda\frac{\partial v_x}{\partial y}+\mu\frac{\partial v_x}{\partial z}. \tag{23}$$

The coefficient λ is determined by the magnitude of the ion flux in the y-boundary region according to

$$\lambda(y)=-\frac{1}{\Phi(y)}\frac{\partial\Phi(y)}{\partial y}. \tag{24}$$

The flux itself is modeled by the function

$$\Phi(y)=\frac{\Phi_0}{2}\left[1-\mathrm{erf}\,\frac{4y}{\Gamma}\right], \tag{25}$$

where Γ stands for the transition width from the central region to the unirradiated area. The error function (erf) allows for ion scattering at the movable aperture, tiny position fluctuations of the movable aperture itself and slight fluctuations of the ion-beam angle Θ due to accelerator drifts. The geometrical setup of the beamline and the automatic beam position controlling system is such that Γ is estimated to be smaller than 50 μm.

The coefficient μ follows from Eqs. (1), (2), and (11) and is given by

$$\mu(z)=-\frac{1}{A_0(z)}\frac{\partial A_0(z)}{\partial z}=-\frac{1}{k_0(z)}\frac{\partial k_0(z)}{\partial z}. \tag{26}$$

1. Shear flow of thin surface layers

In thin amorphous surface layers, S_e is constant across the layer thickness d and, hence, $\mu=0$ in Eqs. (23) and (26). In the ideal case of a perfect aperture with transition width $\Gamma=0$, the coefficient λ also vanishes and Eq. (23) reduces to the Laplace equation

$$0=\frac{\partial^2}{\partial y^2}v_x(y,z)+\frac{\partial^2}{\partial z^2}v_x(y,z). \tag{27}$$

The boundary conditions are given by

$$y\geqslant 0:\quad v_x=0,$$

$$y\to-\infty:\quad v_x=v_x^c,$$

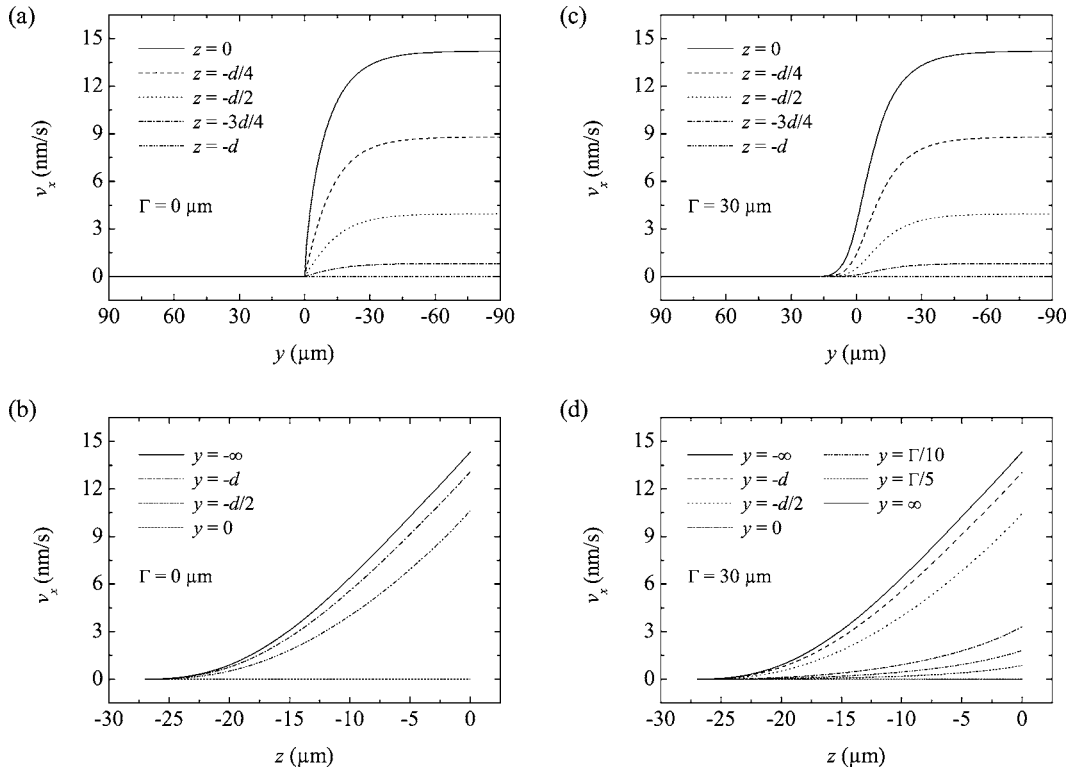

FIG. 9. Steady-state shear velocity $v_x(y,z)$ of the crown glass at the y boundary with a transition width $\Gamma=0$ μm (a) and (b), and $\Gamma=30$ μm (c) and (d), respectively. (a) and (c) show $v_x(y)$ for constant values z and (b) and (d) show $v_x(z)$ for constant values y. All numerical calculations were carried out for an irradiation with 600 MeV Au ions at $T_0=300$ K and ion flux $\Phi_0=4.4\times10^{10}$ cm^{-2} s^{-1}. The maximum deformation length is $\xi_0\sim-40$ μm.

$$z=-d: \quad v_x=0,$$

$$z=0: \quad \sigma_{xz}=0, \tag{28}$$

where $v_x^c(z)=B(z+d)$ denotes the solution in the central region according to Eq. (12), with $B=3A_0\Phi_0\sin 2\Theta$. By means of Eq. (22e), the condition at the surface results in $\partial v_x/\partial z=B$. With these boundary conditions, Eq. (27) can be solved analytically. The solution reads

$$v_x(y,z)=v_x^c(z)+\sum_{n=1}^{\infty} a_n\cos(b_n z)\exp(b_n y), \tag{29}$$

with the coefficients

$$a_n=\frac{-2B}{b_n^2 d}, \quad b_n=(2n-1)\frac{\pi}{2d}. \tag{30}$$

In Figs. 6(a) and 6(b), the solution for $v_x(y,z)$ is shown for the irradiation of our a-Si layers with 350 MeV Au ions at $T_0=80$ K and an ion flux of $\Phi_0=4.6\times10^{10}$ cm^{-2} s^{-1}. The value for A_0 is taken from Table II. From Fig. 6(a) one can see that the transition from $v_x=0$ to $v_x=v_x^c$ occurs within less than $5d$. It is clearly visible that a steady-state shear velocity at the sample surface $v_x(y,z=0)\sim3$ Å/s appears, which smoothly vanishes in the vicinity of the y boundary.

The integration of Eq. (29) over time yields the shift at the specimen surface

$$\Delta x(y,z=0,t)=\Delta x^c(z=0,t)+\sum_{n=1}^{\infty} c_n(t)\exp(b_n y), \tag{31}$$

where $\Delta x^c(z=0,t)=v_x^c(z=0)t=Btd$ denotes the solution for the central region according to Eq. (13) and

$$c_n(t)=a_n t=\frac{-2\Delta x^c(z=0,t)}{b_n^2 d^2}. \tag{32}$$

In Fig. 7 (solid line), the function $\Delta x(y,z=0,t)$ is shown for the irradiation conditions used in Fig. 6 and an ion fluence of $\Phi_0 t=1.7\times10^{15}$ cm^{-2}. In Fig. 8(a), this curve is plotted over a micrograph of the specimen surface taken *in situ* during the experiments. It can be seen that the derived steady-state solution for a y boundary is in good agreement with the observed flow in a-Si. The remaining discrepancies are obviously due to the unknown exact position of $y=0$ and the idealized transition width $\Gamma=0$.

From the solution for v_x given by Eqs. (29) and (30), the macroscopic shear stresses σ_{xy} and σ_{xz} follow by means of Eqs. (22d) and (22e) and read

$$\sigma_{xy}(y,z)=\frac{1}{2k_0\Phi}\sum_{n=1}^{\infty} a_n b_n\cos(b_n z)\exp(b_n y), \tag{33a}$$

$$\sigma_{xz}(y,z) = \frac{-1}{2k_0\Phi}\sum_{n=1}^{\infty} a_n b_n \sin(b_n z)\exp(b_n y). \qquad (33b)$$

The stresses $\sigma_{xy}(0,0)$ and $\sigma_{xz}(0,-d)$ approach $\pm\infty$. This unphysical result is due to the idealized assumption $\Gamma=0$.

The more realistic case is given by $\Gamma>0$. Equation (23) now reads

$$0 = \frac{\partial^2}{\partial y^2}v_x(y,z) + \frac{\partial^2}{\partial z^2}v_x(y,z) + \lambda(y)\frac{\partial}{\partial y}v_x(y,z), \qquad (34)$$

with the boundary conditions

$$y \to \infty: \quad v_x = 0,$$

$$y \to -\infty: \quad v_x = v_x^c,$$

$$z = -d: \quad v_x = 0,$$

$$z = 0: \quad \sigma_{xz} = 0. \qquad (35)$$

Equation (34) can be transformed into a Ricatti differential equation, but we have not found an analytical solution. Therefore, Eq. (34) was solved numerically by using a finite-element code. The reliability of the code was tested by applying it to Eq. (27) with the boundary conditions of Eq. (28). The numerical solution was identical with the analytical one in Eq. (29).

In Figs. 6(c) and 6(d), the results are shown using $\Gamma=30$ μm and the same irradiation conditions as in Figs. 6(a) and 6(b). The shear stresses $\sigma_{xy}(y,z)$ and $\sigma_{xz}(y,z)$ determined by Eqs. (22d) and (22e) remain finite and exhibit a continuous decay in the region $y>0$.

In Fig. 7, the shifts at the surface are shown for various values $\Gamma>0$ in comparison with the corresponding solution for $\Gamma=0$. It can be seen that the total transition width from $\Delta x=0$ to Δx^c does not change dramatically even when $\Gamma=6d$. The transition width represents a convenient fit parameter for the experimentally observed effects. Apparently, the best fit to the underlying micrograph from Fig. 8(a) is given by $\Gamma=10$ μm [Fig. 8(b)].

2. Shear flow of thick layers

In thick amorphous layers, the dependence $S_e(\xi)$ needs to be taken into consideration. Applying Eq. (14) with $S_{e0}=0$, Eq. (26) results in

$$\mu(z) = -\frac{1}{S_e(z)}\frac{\partial S_e(z)}{\partial z} = -\frac{1}{\cos\Theta S_e(\xi)}\frac{\partial S_e(\xi)}{\partial \xi}. \qquad (36)$$

In this way, Eq. (23) has to be solved with Γ as a free parameter and the boundary conditions given by

$$y \geqslant 0 \quad (\Gamma = 0): \quad v_x = 0,$$

$$y \to \infty \quad (\Gamma > 0): v_x = 0,$$

$$y \to -\infty: \quad v_x = v_x^c,$$

$$z = \xi_0 \cos\Theta: \quad v_x = 0,$$

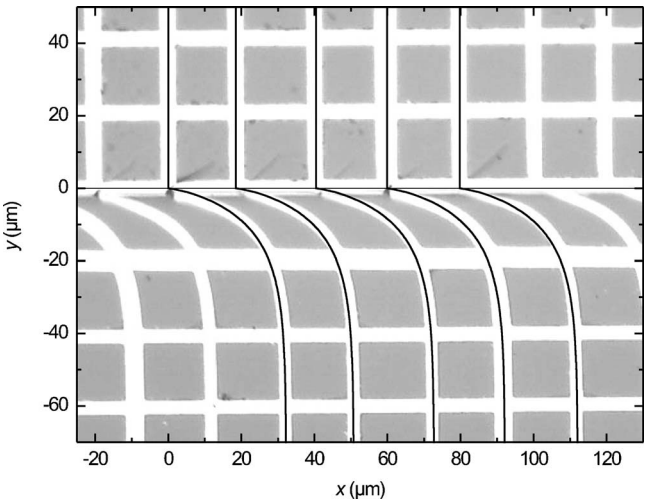

FIG. 10. Comparison of the calculated shift at the surface for a y boundary, $\Delta x(y,z=0,t)$, of the crown glass with the experimental result. The underlying micrograph of the specimen surface was taken after an irradiation with 600 MeV Au ions at $T_0=300$ K, flux $\Phi_0=4.4\times10^{10}$ cm^{-2} s^{-1} and fluence $\Phi_0 t=1\times10^{14}$ cm^{-2}. For the calculation, a transition width $\Gamma=0$ μm was used. The location of $y=0$ was chosen to give optimum agreement with the experiment. The origin of the x scale is arbitrary.

$$z = 0: \quad \sigma_{xz} = 0. \qquad (37)$$

In Fig. 9, the numerical solution of Eq. (23) with the boundary conditions of Eq. (37) is shown for the irradiation of the crown glass with 600 MeV Au ions at $T_0=300$ K and ion flux $\Phi_0=4.4\times10^{10}$ cm^{-2} s^{-1} taking into account a transition width $\Gamma=0$ and $\Gamma=30$ μm, respectively. For the calculations, $S_e(\xi)$ was taken from Fig. 2(b) with $\xi_0=-40$ μm. The value for κ was taken from the experiment (cf. Sec. IV). Similarly to thin layers, the transition from $v_x=0$ to $v_x=v_x^c$ occurs within a distance of less than $5\xi_0$. Because of the larger deformation length in comparison with Γ the transition is somewhat less blurred for the crown glass.

In Fig. 10, a comparison of the numerical result of the shift at the specimen surface $\Delta x(y,z=0,t)$ with the experiment is shown. Because the aperture was not moved during irradiation, we expect $\Gamma<10$ μm. In fact, $\Gamma=0$ yields the best approximation. Although the theoretical approach shows a fairly good description, there are still small discrepancies near the y boundary. These discrepancies cannot be assigned to the unknown exact position of $y=0$. But they could be due to the omitted energy-deposition threshold S_{e0}, the modeling of $A_0(S_e)$ and $k_0(S_e)$, and/or due to the ignorance of the tensorial character of the fluidity.

C. Irradiation effects at the *x* boundaries

At x boundaries any plane parallel to the x-z plane is a symmetry plane. Therefore, the derivatives $\partial/\partial y$ and v_y must vanish everywhere. A closer inspection of Eqs. (4)–(10) shows that σ_{xy} and σ_{yz} must also vanish. The permanent change of shape and size of the ditches and dikes suggests that under the irradiation conditions of this work no steady state is reached. Therefore, the solution of Eqs. (7) and (10)

depends explicitly on time and requires considerable numerical effort.

Abstaining from the precise modeling of the ditch and dike structures, they can be grossly characterized in the following way. Since the plastic flow occurs without material loss and assuming constant mass density, the cross sections of the ditch F_d and dike F_D at the x boundaries as well as that of the laterally transported matter in the central region F_c must be equal. This cross section F_c is determined by the integration of the shift $\Delta x(z,t)$, resulting from Eq. (12), over the entire deformation depth $z_0=\xi_0 \cos \Theta$ according to

$$F_c = \int_{z_0}^{0} \Delta x(z,t) dz = \int_{z_0}^{0} \int_{0}^{t} v_x(z) dt\, dz$$
$$= 3\Phi_0 t \sin 2\Theta \cos \Theta \int_{z_0}^{0} \int_{\xi_0}^{z/\cos \Theta} A_0[S_e(\xi)] d\xi\, dz. \tag{38}$$

For thin surface layers, where S_e=const across the layer thickness, the value F_c reads

$$F_c(t) = \frac{3}{2} d^2 A_0 \Phi_0 t \sin 2\Theta = \frac{d}{2} \Delta x(z=0,t). \tag{39}$$

In Table II, a comparison of the measured values F_d, F_D, and their mean value F_m with F_c is listed for the irradiations of the a-Si samples. It can be seen that the experimental results agree well with the values derived from the viscoelastic model by means of Eq. (39).

Ditch and dike structures have been first observed by Gutzmann *et al.* in the metallic glass $Fe_{40}Ni_{40}B_{20}$,[45,51] and somewhat later by Cliche *et al.* in a variety of amorphous materials.[13,14] The latter authors ascribed the formation of these structures to an effect of momentum conservation and regarded ion hammering as a different phenomenon. However, the agreement of the cross sections in the central region F_c with those at the x boundaries F_m demonstrates clearly that ditch and dike formation is the consequence of shear flow which is a consequence of ion hammering. An additional concept such as momentum transfer is not necessary.

VI. CONCLUSION

The macroscopic plastic flow of thin amorphous surface layers and amorphous bulk materials, which occurred during swift heavy-ion irradiation, was studied experimentally and theoretically within the viscoelastic effective-flow-temperature approach. The experimental investigations were performed using a-Si surface layers and crown glass samples as representatives for both geometry types.

Far away from any symmetry-breaking boundaries, a steady state of ion hammering and irradiation creep occurs after about one complete coverage of the surface area with ion tracks. Depending on material properties and irradiation conditions such as the electronic energy deposition and the ion's incidence angle, this steady state is characterized by a shear velocity in the direction of the projection of the ion beam onto the surface, in-plane stresses, and a constant density of the irradiated material. When a borderline between irradiated and unirradiated specimen parts runs parallel with the shear velocity, flow is hampered and a reduction of the steady-state shear velocity occurs. The width of the transition from zero velocity to fully developed shear flow is determined by the maximum deformation depth and Γ, the transition width of the ion flux. For thin amorphous surface layers and $\Gamma=0$ an analytical description for the lateral shear velocity is given. The case $\Gamma \neq 0$ requires numerical calculations, removes the divergence of shear stresses and ensures excellent agreement with the experimental results. In the case of bulk amorphous materials, the depth dependence of the electronic energy deposition has to be taken into account, since it dominates the location dependence of the shear velocity and the influence of a finite transition width is less pronounced.

At a boundary which runs perpendicular to the shear velocity, a ditch or a dike appears as a result of the homogeneous lateral mass transport. Since the shape of the irradiated boundary region is under permanent change, a steady state cannot be reached. The consistency of the cross sections of ditch and dike as well as that of the uniform flow in the central region shows that no measurable density change in these lateral boundary regions occurs.

In summary, the very good agreement between the analytical and numerical solutions derived from the modified viscoelastic Maxwell model with the experimental results further support the idea of an efficient shear-stress relaxation along the ion path during the thermal spike period. Using general theorems on elasticity[37] the constitutive equation of ion hammering, Eq. (7), imposes rather narrow boundary conditions on the microscopic processes in the ion tracks. The viscoelastic models of Trinkaus and Ryazanov,[15] Trinkaus,[16–19] and van Dillen *et al.*[38] are in full agreement with Eq. (7). However, those models are not undisputed! Unfortunately, alternative models[10,52] are less advanced and, at present, it is not clear whether they lead to the form of constitutive equation as presented by Eq. (7).

ACKNOWLEDGMENTS

The authors thank A. Kamarou and E. Wendler for the experimental support and encouraging discussions, and U. Kaiser and C. Voigt for the contributions to the analysis of the samples.

[1] M. Toulemonde, C. Dufour, and E. Paumier, Phys. Rev. B **46**, 14362 (1992).
[2] M. Toulemonde, J. M. Costantini, C. Dufour, A. Meftah, E. Paumier, and F. Studer, Nucl. Instrum. Methods Phys. Res. B **126**, 37 (1996).
[3] M. Toulemonde, C. Dufour, E. Paumier, and F. Pawlak, Mater. Res. Soc. Symp. Proc. **504**, 99 (1999).
[4] L. Cartz, F. G. Karioris, and R. A. Fournelle, Radiat. Eff. **54**, 57 (1981).
[5] S. Klaumünzer and G. Schumacher, Phys. Rev. Lett. **51**, 1987 (1983).
[6] A. Audouard, E. Balanzat, G. Fuchs, J. C. Jousset, D. Lesueur, and L. Thomé, Europhys. Lett. **3**, 327 (1987).
[7] A. Benyagoub, S. Löffler, M. Rammense, and S. Klaumünzer, Radiat. Eff. Defects Solids **110**, 217 (1989).
[8] S. Klaumünzer, C. Li, S. Löffler, M. Rammense, G. Schumacher, and H. C. Neitzert, Radiat. Eff. Defects Solids **108**, 131 (1989).
[9] S. Klaumünzer, M. D. Hou, and G. Schumacher, Phys. Rev. Lett. **57**, 850 (1986).
[10] G. Szenes, Mater. Sci. Forum **97–99**, 647 (1992).
[11] G. Szenes, Phys. Rev. B **51**, 8026 (1995).
[12] G. Szenes, Nucl. Instrum. Methods Phys. Res. B **107**, 150 (1996).
[13] L. Cliche, S. Roorda, M. Chicoine, and R. A. Masut, Phys. Rev. Lett. **75**, 2348 (1995).
[14] M. Chicoine, S. Roorda, L. Cliche, and R. A. Masut, Phys. Rev. B **56**, 1551 (1997).
[15] H. Trinkaus and A. I. Ryazanov, Phys. Rev. Lett. **74**, 5072 (1995).
[16] H. Trinkaus, J. Nucl. Mater. **223**, 196 (1995).
[17] H. Trinkaus, Nucl. Instrum. Methods Phys. Res. B **107**, 155 (1996).
[18] H. Trinkaus, J. Nucl. Mater. **246**, 244 (1997).
[19] H. Trinkaus, Nucl. Instrum. Methods Phys. Res. B **146**, 204 (1998).
[20] M. D. Hou, S. Klaumünzer, and G. Schumacher, Phys. Rev. B **41**, 1144 (1990).
[21] S. Klaumünzer, Mater. Sci. Forum **97–99**, 623 (1992).
[22] A. Audouard, E. Balanzat, J. C. Jousset, D. Lesueur, and L. Thomé, J. Phys.: Condens. Matter **5**, 995 (1993).
[23] A. Benyagoub, S. Klaumünzer, and M. Toulemonde, Nucl. Instrum. Methods Phys. Res. B **146**, 449 (1998).
[24] A. Gutzmann, S. Klaumünzer, and P. Meier, Phys. Rev. Lett. **74**, 2256 (1995).
[25] H. Narayan, S. B. Samanta, H. M. Agrawal, R. P. S. Kushwaha, D. Kanjilal, S. K. Sharma, and A. V. Narlikar, J. Phys.: Condens. Matter **11**, 2679 (1999).
[26] H. Narayan, H. M. Agrawal, R. P. S. Kushwaha, D. Kanjilal, and S. K. Sharma, Nucl. Instrum. Methods Phys. Res. B **156**, 217 (1999).
[27] H. Narayan, S. B. Samanta, H. M. Agrawal, R. P. S. Kushwaha, A. Gupta, S. K. Sharma, A. V. Narlikar, and D. Kanjilal, Nucl. Instrum. Methods Phys. Res. B **196**, 89 (2002).
[28] E. Snoeks, A. van Blaaderen, T. van Dillen, C. M. van Kats, M. L. Brongersma, and A. Polman, Adv. Mater. (Weinheim, Ger.) **12**, 1511 (2000).
[29] E. Snoeks, A. van Blaaderen, T. van Dillen, C. M. van Kats, K. Velikov, M. L. Brongersma, and A. Polman, Nucl. Instrum. Methods Phys. Res. B **178**, 62 (2001).
[30] T. van Dillen, A. van Blaaderen, W. Fukarek, and A. Polman, Appl. Phys. Lett. **78**, 910 (2001).
[31] T. van Dillen, E. Snoeks, W. Fukarek, C. M. van Kats, A. van Blaaderen, and A. Polman, Nucl. Instrum. Methods Phys. Res. B **175–177**, 350 (2001).
[32] T. van Dillen, M. J. A. de Dood, J. J. Penninkhof, A. Polman, S. Roorda, and A. M. Vredenberg, Appl. Phys. Lett. **84**, 3591 (2004).
[33] S. Klaumünzer, Nucl. Instrum. Methods Phys. Res. B **215**, 345 (2004).
[34] J. C. Cheang-Wong, U. Morales, A. Olivier, L. Rodríguez-Fernández, and J. Rickards, Nucl. Instrum. Methods Phys. Res. B (to be published).
[35] A. Hedler, S. Klaumünzer, and W. Wesch, Nat. Mater. **3**, 804 (2004).
[36] J. D. Eshelby, Proc. R. Soc. London, Ser. A **241**, 376 (1957).
[37] T. Mura, *Micromechanics of Defects in Solids*, 2nd ed. (Martinus Nijhoff Publishers, Dordrecht, 1987).
[38] T. van Dillen, A. Polman, P. R. Onck, and E. van der Giessen, Phys. Rev. B **71**, 024103 (2005).
[39] The penetration path ξ is counted negative, with $\xi=0$ at the surface, in order to be compatible with the depth z, so that $z=\xi\cos\Theta$.
[40] S. Klaumünzer, Nucl. Instrum. Methods Phys. Res. B **225**, 136 (2004).
[41] See, e.g., W. Wesch, A. Kamarou, and E. Wendler, Nucl. Instrum. Methods Phys. Res. B **225**, 111 (2004).
[42] M. L. Brongersma, E. Snoeks, T. van Dillen, and A. Polman, J. Appl. Phys. **88**, 59 (2000).
[43] E. Snoeks, A. Polman, and C. A. Volkert, Appl. Phys. Lett. **65**, 2487 (1994).
[44] E. Snoeks, W. Weber, A. Cacciato, and A. Polman, J. Appl. Phys. **78**, 4723 (1995).
[45] A. Gutzmann and S. Klaumünzer, Nucl. Instrum. Methods Phys. Res. B **127/128**, 12 (1997).
[46] S. Klaumünzer, in *Multiscale Phenomena in Plasticity*, Vol. 367 of NATO Advanced Study Institute, Series E: Applied Sciences, edited by J. Lépinoux *et al.* (Kluwer, The Netherlands, 2000), pp. 441–450.
[47] J. S. Custer, M. O. Thompson, D. C. Jacobson, J. M. Poate, S. Roorda, W. C. Sinke, and F. Spaepen, Appl. Phys. Lett. **64**, 437 (1994).
[48] C. A. Volkert, J. Appl. Phys. **70**, 3521 (1991).
[49] J. F. Ziegler, J. P. Biersack, and U. Littmark, *The Stopping and Range of Ions in Solids* (Pergamon Press, New York, 2003).
[50] A. Hedler, S. Klaumünzer, and W. Wesch, Nucl. Instrum. Methods Phys. Res. B (to be published).
[51] A. Gutzmann, S. Klaumünzer, A. Benyagoub, and D. Nagengast, Radiat. Eff. Defects Solids **126**, 133 (1993).
[52] V. A. Borodin, A. E. Volkov, and D. N. Korolev, Nucl. Instrum. Methods Phys. Res. B **209**, 122 (2003).